Trajectory Approximation of a Passively Actuated Solar Balloon in Near-Earth Mission Scenarios

Marco Bassetto*, Alessandro A. Quarta, Giovanni Mengali

Dipartimento di Ingegneria Civile e Industriale, University of Pisa, Italy

Abstract

The aim of this paper is to investigate the heliocentric motion of a passively actuated solar balloon placed at a distance of about one astronomical unit from the Sun. The analysis exploits a recent thrust model, according to which a solar balloon undergoes a passive control of its lightness number (that is, the ratio of the generated thrust to the local weight of the entire spacecraft) in the form a proportional feedback controller of constant gain. The spacecraft trajectory is obtained with a regularization of the equations of motion, in such a way that the heliocentric dynamics of the passively actuated solar balloon becomes equivalent to that of a nonlinear oscillator with a single degree of freedom. The approximate solution available for this type of nonlinear oscillator is then used to accurately describe the heliocentric motion of the passively actuated solar balloon and to analyze a couple of mission scenarios, that is, the execution of a phasing maneuver on an elliptical working orbit and the rotation of the apse line of the osculating orbit.

Keywords: passively actuated solar balloon, trajectory approximation, near-Earth orbits, solar sail

Nomenclature

a	=	semimajor axis, [au]
$\boldsymbol{a}$	=	propulsive acceleration vector, [mm/s^2]
a_r	=	propulsive acceleration magnitude, [mm/s^2]
$\{A,\,B\}$	=	constant coefficients
e	=	eccentricity
$\boldsymbol{e}$	=	eccentricity vector
E	=	eccentric anomaly, [deg]
$\mathcal{E}$	=	specific mechanical energy, [m^2/s^2]
El	=	Young's modulus, [Pa]
f	=	natural frequency; see Eq. (32)
F	=	function of y; see Eq. (22)
g	=	auxiliary function; see Eq. (50)
G	=	primitive function; see Eq. (49)
h	=	auxiliary function; see Eqs. (4)
H	=	conserved quantity; see Eq. (23)
$\hat{\boldsymbol{i}}_r$	=	radial unit vector

*Corresponding author

Email addresses: `marco.bassetto@ing.unipi.it` (Marco Bassetto), `a.quarta@ing.unipi.it` (Alessandro A. Quarta), `g.mengali@ing.unipi.it` (Giovanni Mengali)

$\hat{\boldsymbol{i}}_t$	=	transverse unit vector
k	=	constant gain, $[\text{au}^{-1}]$
$\tilde{k}$	=	dimensionless gain; see Eqs. (11)
n	=	number of moles
O	=	Sun's center of mass
p	=	semilatus rectum, [au]
P	=	balloon's internal gas pressure, [Pa]
q	=	thickness of the shell, [m]
r	=	Sun-spacecraft distance, [au]
R	=	balloon's radius, [m]
$\mathcal{R}$	=	universal gas constant, $[\text{J}/(\text{K}\,\text{mol})]$
$r_{\oplus}$	=	reference distance, [au]
S	=	spacecraft center of mass
t	=	time, [years]
T	=	balloon's internal gas temperature, $[^{\circ}\text{C}]$
$\mathcal{T}$	=	polar reference frame
$\mathcal{T}_I$	=	inertial reference frame
u	=	radial component of the spacecraft velocity, [km/s]
V	=	balloon's volume, $[\text{m}^3]$
x	=	auxiliary variable; see Eq. (8)
y	=	auxiliary variable; see Eq. (12)
y_C	=	center of oscillation
$\{\alpha_1,\,\alpha_2,\,\alpha_3,\}$	=	constant coefficients; see Eqs. (33)
β	=	lightness number
γ	=	E-sail performance parameter
ϵ_r	=	relative error in position
ϵ_t	=	relative error in time
θ	=	polar angle, [rad]
Λ	=	dimensionless constant coefficient; see Eq. (14)
$\mu_{\odot}$	=	Sun's gravitational parameter, $[\text{km}^3/\text{s}^2]$
$\tilde{\mu}$	=	dimensionless gravitational parameter; see Eqs. (11)
ν	=	true anomaly, [deg]
ρ	=	Poisson's ratio
τ	=	thermal expansion coefficient, $[^{\circ}\text{C}^{-1}]$
ϕ	=	phasing angle, [deg]
$\Delta\omega$	=	precession of the osculating orbit apse line, [deg]

Subscripts

eq	=	equivalent
f	=	final
max	=	maximum
min	=	minimum
0	=	at $t = t_0$
$\oplus$	=	at $r = r_{\oplus}$

Superscripts

$\cdot$	=	derivative with respect to t
$'$	=	derivative with respect to θ
$\wedge$	=	approximate
$-$	=	limiting value
$\sim$	=	at $r = \tilde{r}$
$\star$	=	target value

1. Introduction

A solar balloon is a spherical solar sail consisting of a thin shell inflated with a suitable gas and externally coated with a highly reflective material. The original concept of a solar balloon dates back to 1960 and is related to NASA's Project Echo [1, 2, 3], the first ever passive communications satellite experiment, which was also useful for evaluating the perturbative effects of the solar radiation pressure in a low-Earth orbit [4]; see Fig. 1.
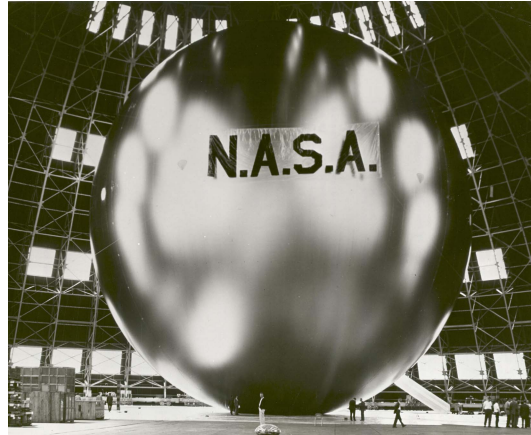
(a) Tensile stress test in a dirigible hangar. Image Credit: NASA
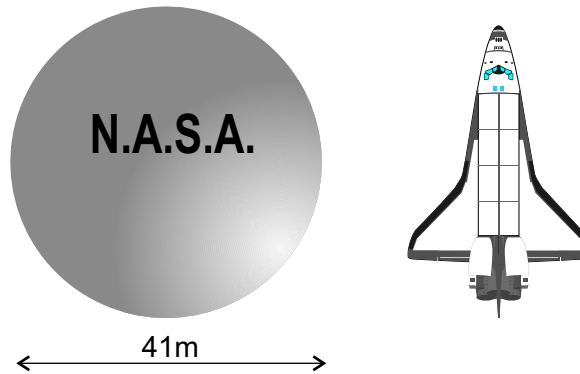
(b) Characteristic dimensions.

Figure 1: NASA's solar balloon Echo II

Like a Sun-facing solar sail, a solar balloon can only generate an outward radial propulsive acceleration, which means that its thrust vector is always aligned with the local Sun-spacecraft (or radial) direction and points away from the Sun. In a heliocentric mission scenario, the working principle of a passively actuated solar balloon (PASB) is based on the alternate expansion and contraction of the thin shell when the balloon either moves towards the Sun or away from it, respectively. More precisely, when it shifts towards the Sun, the PASB undergoes an expansion due to the increase in temperature, which in turn raises the area exposed to the Sun and so increases the solar radiation pressure force. Vice versa, a displacement away from the Sun reduces the exposed area and decreases the magnitude of the generated thrust. Like a flat solar sail, the performance of a solar balloon may be described by the lightness number β, a dimensionless positive parameter defined as the ratio of the propulsive acceleration magnitude to the local Sun's gravitational acceleration. In this paper, the lightness number is assumed to be a constant parameter. Actually, due to thermal degradation effects, its value tends to decrease over time and to progressively reduce the performance

of the solar balloon [5, 6, 7]. Moreover, this work does not even consider wrinkles and creases, which may be seen as degrading effects as well [8].

The peculiarity of a PASB is that it undergoes a so-called "passive β-control" in the form $\delta\beta = -k\,\delta r$, where $\delta\beta$ is the change in lightness number, k is a positive gain, and δr is the spacecraft displacement along the Sun-spacecraft line [9]. In principle, a sort of "active β-control" could be obtained with a suitable device capable of inflating/deflating the solar balloon, or by coating its external surface with materials that can vary their reflectivity in a controlled way. In this regard, a possible option is to coat the external surface with electrochromic materials, that is, materials with the capability of changing their optical characteristics upon the application of an electrical voltage [10, 11, 12, 13, 14].

For practical purposes, a PASB is a promising option to stabilize an Earth-Sun L_1-type artificial equilibrium point with a passive β-control, provided that k is greater than a minimum threshold value [9]. This problem has been also recently addressed by Vulpetti et al. [15], who investigated the possibility of obtaining an early warning of solar storms caused by coronal mass ejection by means of a satellite maintained at an artificial equilibrium point using a solar sail. In the context of PASBs, Aliasi et al. [16] investigated the feasibility of stabilizing a collinear artificial Lagrangian point at linear order. It was found that a PASB can only stabilize L_1-type artificial equilibrium points sufficiently close to the Sun. However, since these equilibrium points require considerable values of β (i.e., values that are beyond the current level of technological development) and high operational temperatures [16], they are not accessible in practice. In fact, typical values of β are much smaller than unity; see for example some solar sail-based missions such as the JAXA's Interplanetary Kite-craft Accelerated by Radiation Of the Sun (IKAROS) [17, 18, 19], the NASA's NanoSail-D2 [20], or the Planetary Society's LightSail 1 [21, 22] and LightSail 2 [23], for which the order of magnitude of β ranges between 10^{-3} and 10^{-2}. Instead, L_1-type equilibrium points not so close to the Sun cannot be stabilized due to the limitations on k. The actual value of k depends on a number of parameters such as the Poisson's ratio, the Young's modulus, the thermal expansion coefficient of the shell material, and the physical and molecular characteristics of the enclosed gas. According to Ref. [16] the required values of k could be obtained with thermal expansion coefficients that are well beyond the current technology level. On the other hand, all those problems may be overcome with an active control of the lightness number. In this regard, Aliasi et al. [24], investigated the control of artificial Lagrangian points in the Alpha Centauri A and B star system by means of an actively actuated solar balloon. With a linear stability analysis, the authors [24] showed that, in some cases, the artificial equilibrium points can be stabilized with a simple feedback control law based on an active β-control.

The aim of this paper is to analyze the heliocentric motion of a PASB starting from the propulsive acceleration model proposed in Ref. [16]. In particular, the trajectory analysis is carried out through a regularization of the equations of motion, which allows the PASB dynamics to be made equivalent to a nonlinear oscillator with a single degree of freedom [25, 26]. An approximate solution, originally found by Nayfeh and Mook for this type of nonlinear oscillator [27], is here exploited to accurately describe the heliocentric trajectory of a PASB. Moreover, a set of mission scenarios are analyzed within the limits of applicability of the adopted thrust model [16]. The novelty of this paper is twofold. First, we provide an analytical approximation of the heliocentric trajectory of a PASB. In particular, through a suitable change of variable, the heliocentric dynamics of a PASB is shown to be similar to that of a spinning Electric Solar Wind Sail (E-sail) with a Sun-facing attitude [28, 29, 30]. Secondly, we explore the capabilities of a PASB in a couple of near-Earth mission scenarios different from the generation of an artificial equilibrium point [15, 31, 32].

The paper is organized as follows. Section 2 deals with the mathematical model that is used for describing the orbital dynamics of a PASB in a near-Earth mission scenario. Section 3 presents the approximate heliocentric trajectory and Section 4 discusses its validation through a comparison of the approximate results with those obtained by a numerical propagation of the equations of motion. Section 5 investigates the performance of a PASB in two mission scenarios, that is, a phasing maneuver on an elliptical working orbit and the rotation of the apse line of the osculating orbit. Finally, Section 6 contains some concluding remarks.

4

2. Mathematical model

Consider a PASB S that, at the initial time $t = t_0 \triangleq 0$, is covering a heliocentric parking orbit of semilatus rectum p_0 and eccentricity $e_0 < 1$. Introduce a heliocentric polar reference frame $\mathcal{T}(O; \hat{\boldsymbol{i}}_r, \hat{\boldsymbol{i}}_\theta)$, where the origin O coincides with the Sun's center of mass, $\hat{\boldsymbol{i}}_r$ is the radial (i.e., Sun-spacecraft) unit vector, while $\hat{\boldsymbol{i}}_\theta$ is the transverse unit vector, which lies on the parking orbit plane and points in the same direction as the inertial velocity of the PASB. The spacecraft position is described through the orbital radius r and the polar angle θ, that is, the angle (measured counterclockwise on the orbital plane) between the Sun-spacecraft unit vector $\hat{\boldsymbol{r}}$ and the Sun-spacecraft line at the initial time t_0; see Fig. 2.
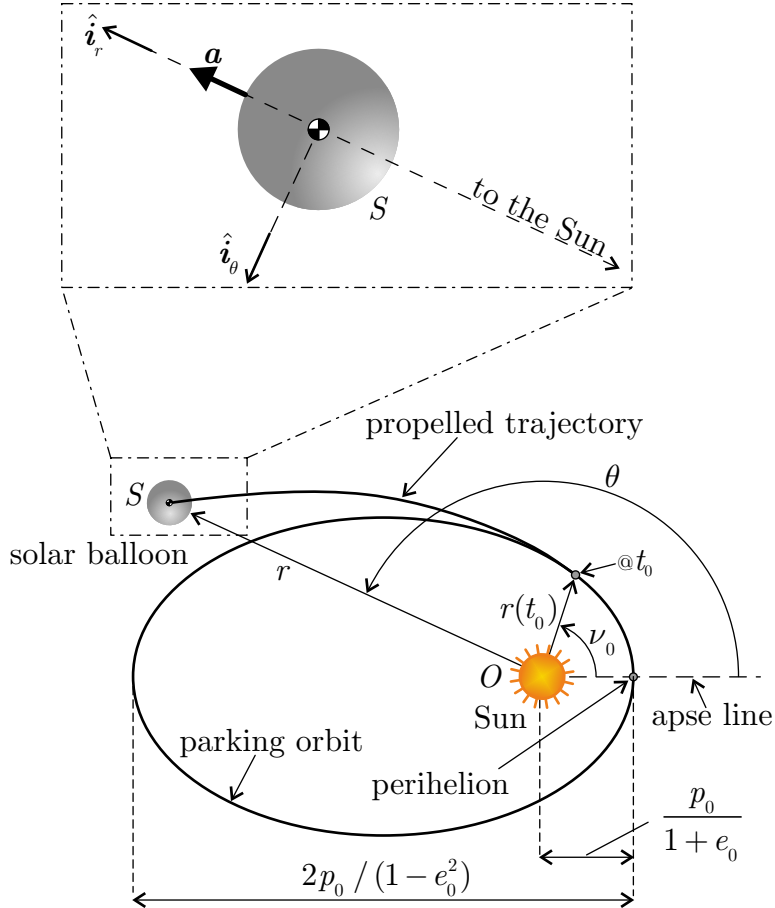

Figure 2: Reference frame and parking orbit characteristics.

2.1. PASB thrust model

The propulsive acceleration vector provided by a PASB may by written as

$$\boldsymbol{a} = a_r \, \hat{\boldsymbol{i}}_r \qquad \text{with} \qquad a_r \triangleq \beta \, \frac{\mu_\odot}{r^2} > 0 \tag{1}$$

where $\mu_\odot \simeq 1.3271 \times 10^{11} \, \text{km}^3/\text{s}^2$ is the Sun's gravitational parameter. The value of the lightness number β depends on a number of physical characteristics such as the total spacecraft mass, the optical properties of the reflective film, and the actual diameter of the balloon. Using the simplified mathematical model described in Ref. [16], the lightness number of a PASB can be written as a function of r as
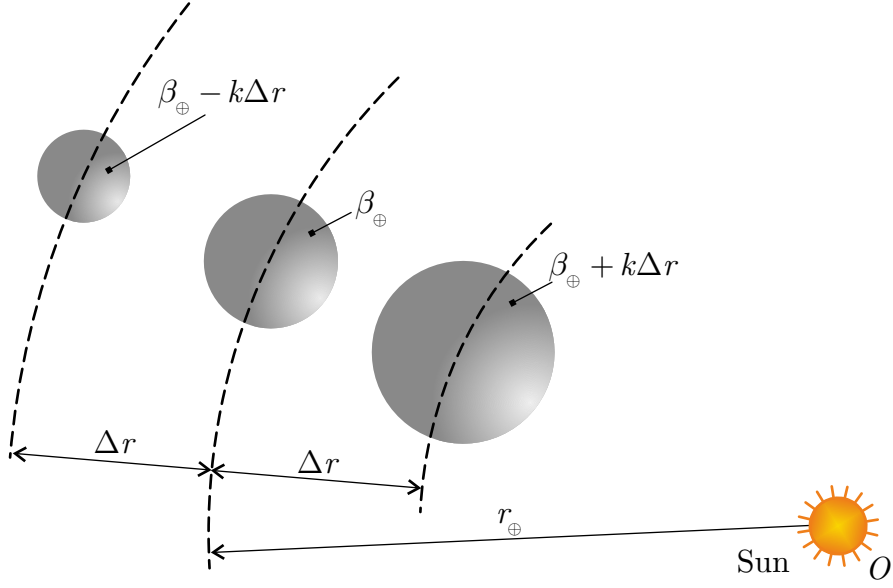
$$\beta = \beta_\oplus - k \, (r - r_\oplus) \tag{2}$$

Figure 3: Conceptual sketch of the PASB behaviour in a near-Earth mission scenario.

where $r_\oplus \triangleq 1\,\text{au}$ is a reference distance and $\beta_\oplus > 0$ is the lightness number when $r = r_\oplus$. Figure 3 shows a conceptual sketch of the behaviour of a PASB, where $\Delta r \triangleq |r - r_\oplus|$.

Note that, in principle, Eq. (2) contemplates negative or null values of β when

$$r \geq \frac{\beta_\oplus + k\,r_\oplus}{k} \tag{3}$$

Since those values are not physically feasible, the trajectory analysis must be limited to the cases in which $\beta > 0$. Also recall that the thrust model can only be applied to heliocentric distances of about one astronomical unit [16].

Rearranging Eq. (22) of Ref. [16] when $r \simeq r_\oplus$, the dimensionless product $k\,r_\oplus$ may be written as

$$k\,r_\oplus = \left(\frac{\widetilde{h} + \tau\,\widetilde{T}}{1 + 3\,\widetilde{h}}\right) \frac{\widetilde{\beta}}{\widetilde{r}/r_\oplus} \qquad \text{with} \qquad \widetilde{h} \triangleq \frac{1 - \rho}{El}\,\frac{\widetilde{P}\,\widetilde{R}}{2\,q} \tag{4}$$

where the superscript $\sim$ indicates that the generic variable corresponds to when $r = \widetilde{r}$. In Eq. (4), ρ is the Poisson's ratio, El is the Young's modulus, P is the pressure of the enclosed gas, R is the balloon radius, q is the shell thickness, τ is the thermal expansion coefficient of the shell material, and T is the gas temperature. The latter, in turn, depends on the incoming solar thermal power and on the optical properties of the reflective surface (through the absorption and emissivity coefficients) and affects the gas pressure P, the balloon's radius R, and, ultimately, the value of h; see Eq. (4).

For example, Aliasi et al. [16] estimated that $k\,r_\oplus \simeq 2.6 \times 10^{-4}$ when the shell is made of Kapton (that is, when $\rho = 0.34$, $El = 2.5 \times 10^9\,\text{Pa}$, and $\tau = 2 \times 10^{-5}\,°\text{C}^{-1}$), $\widetilde{P}\,\widetilde{R}/(2\,q) = 7 \times 10^4\,\text{Pa}$, $\widetilde{T} \simeq 252\,°\text{C}$, $\widetilde{r} = 0.9804\,r_\oplus$, and $\widetilde{\beta} = 0.05$. Note that, because of the assumption of perfect gas [16], the number of moles n may be calculated from the knowledge of the balloon's radius as

$$n = \frac{\widetilde{P}\,\widetilde{V}}{\mathcal{R}\,\widetilde{T}} \tag{5}$$

where $\widetilde{V} \triangleq 4\,\pi\,(\widetilde{R})^3/3$ is the balloon's volume and $\mathcal{R} \simeq 8.3145\,\text{J}/(\text{K mol})$ is the universal gas constant. Using the data of Ref. [16] and assuming $\widetilde{R} = 20.55\,\text{m}$ and $q = 18\,\mu\text{m}$ (the design parameters of NASA's Echo II [33]), we get $\widetilde{P} \simeq 0.1226\,\text{Pa}$ and $n \simeq 1.0193\,\text{mol}$. Instead, when $\widetilde{r} = r_\oplus$ (i.e., $\widetilde{\beta} \equiv \beta_\oplus$), $\widetilde{R} = 20.55\,\text{m}$,

$n = 1\,\mathrm{mol}$, $\widetilde{T} = 250\,^\circ\mathrm{C}^{-1}$, $q = 18\,\mu\mathrm{m}$, and the shell is made of Kapton, we get $k\,r_\oplus \simeq 5 \times 10^{-3}\,\beta_\oplus$. Although $k\,r_\oplus$ depends on many parameters, such as the shell material, the size of the PASB, the optical properties of its external surface, and the properties of the enclosed gas, without loss of generality we can reasonably assume that the product $k\,r_\oplus$ can vary between 0 and $\beta_\oplus/100$. In particular, the limiting case $k = 0$ models the behaviour of an ideal Sun-facing solar sail or a Smart Dust [34, 35, 12] with constant optical properties [7, 36, 37].

2.2. PASB equations of motion

Since a solar balloon can only generate an outward radial propulsive acceleration, the semilatus rectum p of the osculating orbit is a constant of motion (i.e., $p = p_0$ for all $t \geq t_0$). Accordingly, the equations describing the heliocentric motion of a PASB at a distance of about one astronomical unit from the Sun are

$$\dot{r} = u \quad , \quad \dot{u} = -\frac{\mu_\odot}{r^2} + \frac{\mu_\odot\,p_0}{r^3} + a_r \quad , \quad \dot{\theta} = \frac{\sqrt{\mu_\odot\,p_0}}{r^2} \tag{6}$$

where the dot symbol denotes a derivative taken with respect to the time t, u is the radial component of the spacecraft velocity, and a_r is given by Eq. (1). Equations (6) are completed by the initial conditions

$$r(t_0) = r_0 \triangleq \frac{p_0}{1 + e_0\,\cos\nu_0} \quad , \quad u(t_0) = u_0 \triangleq \sqrt{\frac{\mu_\odot}{p_0}}\,e_0\,\sin\nu_0 \quad , \quad \theta(t_0) = 0 \tag{7}$$

where ν_0 is the spacecraft true anomaly on the parking orbit at t_0; see Fig. 2. According to Eqs. (6), the dynamics of a PASB is equivalent to that of a spacecraft subject to a continuous radial propulsive acceleration, which is inversely proportional to the orbital radius. In this case, the resulting trajectory may be conveniently analyzed with an approach useful for investigating the effect of a conservative perturbative radial acceleration on the motion of a spacecraft in a two-body gravitational field. In particular, the next section deals with a regularization of the two-body motion [25, 26, 38], through which Eqs. (6)-(7) are rewritten in the form of an equivalent nonlinear oscillator with a single degree of freedom.

2.3. Regularization of the equations of motion

Equations (6) are rearranged in a more compact form by introducing the auxiliary dimensionless variable $x < 1$, defined as

$$x \triangleq 1 - \frac{p_0}{r} \tag{8}$$

and using θ as the independent variable. The transformation defined in Eq. (8) is consistent with the regularization of the two-body motion described by Burdet and Ferrándiz [25, 26]. In the past, the same change of variables has been successfully exploited to analyze the trajectory of a spacecraft subject to a series of radial and tangential impulses [39], to a constant radial propulsive acceleration [40], or to the propulsive acceleration provided by a Sun-facing E-sail [29, 30].

From Eqs. (6) and (8), the radial velocity u and its time derivative $\dot{u}$ can be written as

$$u = \sqrt{\frac{\mu_\odot}{p_0}}\,x' \quad , \quad \dot{u} = \frac{\mu_\odot}{p_0^2}\,(1 - x)^2\,x'' \tag{9}$$

where the prime symbol denotes a derivative taken with respect to the polar angle θ. Bearing in mind Eqs. (8)-(9), Eqs. (6)-(7) give

$$x'' = 1 - \tilde{\mu} - x - \frac{\tilde{k}}{1 - x} \quad , \quad x'(0) = x_0' \triangleq e_0\,\sin\nu_0 \quad , \quad x(0) = x_0 \triangleq -e_0\,\cos\nu_0 \tag{10}$$

where $\{\tilde{\mu}, \tilde{k}\}$ are two dimensionless constants of motion, defined as

$$\tilde{\mu} \triangleq 1 - \beta_\oplus - k\,r_\oplus \quad , \quad \tilde{k} \triangleq k\,p_0 \tag{11}$$

The first of Eqs. (10) may be further simplified by introducing the auxiliary variable $y < 1$, defined as

$$y \triangleq \frac{x + \tilde{\mu} - 1}{\tilde{\mu}} \tag{12}$$

7

so that the PASB dynamics reduces to

$$y'' = -y + \frac{\Lambda}{1-y} \quad , \quad y'(0) = y_0' \triangleq \frac{e_0 \sin \nu_0}{\tilde{\mu}} \quad , \quad y(0) = y_0 \triangleq 1 - \frac{1 + e_0 \cos \nu_0}{\tilde{\mu}} \tag{13}$$

where $\Lambda \leq 0$ is another constant of motion, given by

$$\Lambda \triangleq -\frac{\tilde{k}}{\tilde{\mu}^2} \tag{14}$$

which ranges (depending on the value of k) between a minimum negative value and zero. Figure 4 shows the variation of $\min(\Lambda)$ as a function of p_0 and $\beta_\oplus$ when $k \, r_\oplus \in [0, \beta_\oplus/100]$. Note that, as long as $p_0 \simeq r_\oplus$, it is found that $|\Lambda| \ll 1$ for all values of $\beta_\oplus$ consistent with the current level of technological development [17, 18, 19, 20, 21, 22, 23]. This result will be useful later to obtain a simplified expression of the heliocentric trajectory of a PASB in a near-Earth mission scenario.
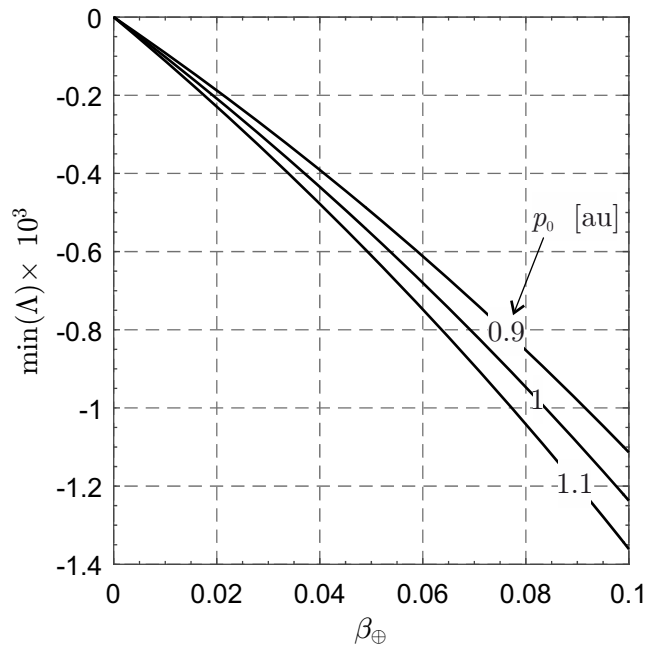

Figure 4: Variation of $\min(\Lambda)$ as a function of p_0, $\beta_\oplus$, and $k \, r_\oplus \in [0, \beta_\oplus/100]$.

In particular, when $\Lambda = 0$ (that is, when $k = 0$, $\tilde{k} = 0$ and $\tilde{\mu} = 1 - \beta_\oplus$), Eq. (13) describes a harmonic oscillator with unitary natural frequency, the solution of which is

$$y = -\frac{\beta_\oplus + e_0 \cos \nu_0}{1 - \beta_\oplus} \cos \theta + \frac{e_0 \sin \nu_0}{1 - \beta_\oplus} \sin \theta \tag{15}$$

In that case, the PASB behaves like a Sun-facing solar sail and the spacecraft trajectory relative to the Sun is a conic section. Indeed, from Eq. (15)

$$r = \frac{p_{\text{eq}}}{1 + e_{\text{eq}} \cos \nu_{\text{eq}}} \tag{16}$$

with

$$p_{\text{eq}} \triangleq \frac{p_0}{\tilde{\mu}} \quad , \quad e_{\text{eq}} \triangleq \frac{\sqrt{e_0^2 + \beta_\oplus^2 + 2 \, e_0 \, \beta_\oplus \, \cos \nu_0}}{1 - \beta_\oplus} \quad , \quad \nu_{\text{eq}} \triangleq \theta + \arctan2 \, (e_0 \sin \nu_0, \, \beta_\oplus + e_0 \, \cos \nu_0) \tag{17}$$

is the polar equation of a conic section with semilatus rectum p_{eq}, eccentricity e_{eq}, and true anomaly ν_{eq}.

8

In the general case when $\Lambda < 0$, Eq. (13) states that the polar form of the PASB heliocentric trajectory (i.e., the function $r = r(\theta)$) can be obtained by analyzing an equivalent nonlinear oscillator with a single degree of freedom (i.e., the state y). According to Nayfeh and Mook [27], the first of Eqs. (13) describes the oscillation of a moving wire with constant mass m and length L, which is crossed by a steady electrical current i_1. The wire is constrained by a linear elastic spring with constant stiffness k_{el} and is subject to the (attractive) magnetic force exerted by a fixed wire of equal length and crossed by a steady electrical current i_2 flowing in the opposite direction than i_1. The situation is illustrated in Fig. 5, where l is the rest spring length, $d > l$ is the (constant) distance between the left constraint and the fixed wire, and $s \in [-l, d-l)$ represents the displacement of the moving wire.
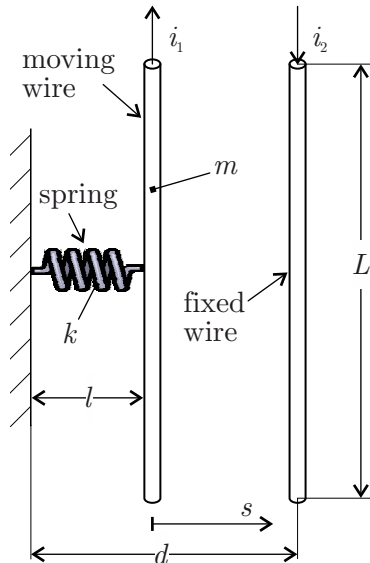

Figure 5: Current-carrying wire subjected to the magnetic force of a current-carrying conductor and to the restoring force of a spring. Adapted from Ref. [27].

The dynamics of the oscillating wire of Fig. 5 is described by the second-order differential equation [27]

$$\frac{\mathrm{d}^2 \sigma}{\mathrm{d}\zeta^2} = -\sigma + \frac{\lambda}{1 - \sigma} \tag{18}$$

where

$$\sigma \triangleq \frac{s}{d - l} \quad , \quad \lambda \triangleq \frac{\mu_0 \, i_1 \, i_2 \, L}{2 \, \pi \, k_{\mathrm{el}} \, (d - l)^2} \quad , \quad \zeta \triangleq \sqrt{\frac{k_{\mathrm{el}}}{m}} \, t \tag{19}$$

and $\mu_0 \equiv 4\pi \times 10^{-7}$ H/m is the vacuum permeability. Since λ is a negative constant (because the two currents i_1 and i_2 have opposite signs), Eq. (18) is formally equivalent to the first of Eqs. (13). The analytical results for this particular nonlinear oscillator [27, 41, 42] may therefore be used to describe the heliocentric trajectory of a PASB. Note also that Eqs. (13) are formally equivalent to Eqs. (4) of Ref. [29], that is

$$x'' = -x + \frac{\gamma}{1 - x} \quad , \quad x'(0) = e_0 \sin \nu_0 \quad , \quad x(0) = -e_0 \cos \nu_0 \tag{20}$$

which represent the heliocentric motion of a Sun-facing E-sail, where $\gamma \triangleq a_c \, r_{\oplus} \, p_0 / \mu_{\odot} \geq 0$ is the E-sail performance parameter (being a_c the E-sail characteristic acceleration), while x is defined as in Eq. (8). Despite such an analogy, the resulting trajectories will be different because of the opposite sign of the forcing terms (in fact, $\gamma \geq 0$ and $\Lambda \leq 0$) and, also, since $y \neq x$; see Eq. (12).

9

2.4. Characteristics of the equivalent nonlinear oscillator

The first integral of the (autonomous) differential equation (13) is

$$\frac{(y')^2}{2} + F(y) = H \tag{21}$$

where

$$F(y) \triangleq \frac{y^2}{2} + \Lambda \ln(1 - y) \tag{22}$$

is a dimensionless function of y, while H is a constant of motion that depends on the initial conditions and on the physical properties of the PASB, viz.

$$H \triangleq \frac{(y_0')^2}{2} + \frac{y_0^2}{2} + \Lambda \ln(1 - y_0) \tag{23}$$

Note that Eq. (23) reduces to

$$H = \frac{1}{2}\left(1 - \frac{1}{\tilde{\mu}}\right)^2 - \Lambda \ln(\tilde{\mu}) \tag{24}$$

when the parking orbit is circular (i.e., when $e_0 = 0$) and, as such, $y_0' = 0$ and $y_0 = (1 - 1/\tilde{\mu})$; see Eqs. (13).

The left-hand side of Eq. (21) is therefore a conserved quantity of the dynamical system described by Eqs. (13). Since $(y_0')^2/2$ is always non-negative, the function $F(y)$ ranges between a minimum, that is, $F_{\min} \triangleq H - \max\left\{(y')^2/2\right\}$ and a maximum, that is, $F_{\max} = H$. In particular, the expression of $F_{\min}$ may be calculated by enforcing the necessary condition

$$\frac{\partial F(y)}{\partial y} = 0 \tag{25}$$

from which

$$y = y_C \triangleq \frac{1}{2} - \sqrt{\frac{1}{4} - \Lambda} \tag{26}$$

so that

$$F_{\min} = \frac{1}{2}\left(\frac{1}{2} - \sqrt{\frac{1}{4} - \Lambda} - \Lambda\right) + \Lambda \ln\left(\frac{1}{2} + \sqrt{\frac{1}{4} - \Lambda}\right) \tag{27}$$

The graph of the function $F_{\min} = F_{\min}(\Lambda)$ is reported in Fig. 6, which clearly shows that $F_{\min} < 0$ (or $F_{\min} = 0$) when $\Lambda < 0$ (or $\Lambda = 0$).

From a physical point of view, the function $F = F(y)$ is minimum when the absolute value of the radial velocity is maximum (and, therefore, the radial acceleration is zero), while it is maximum when the radial velocity is zero (and, therefore, the absolute value of the radial acceleration is maximum). In other words, the motion of the PASB, both when described on the plane of the dimensionless variables or on the (r, θ) plane, is constrained within an annular region. The values of y that delimit the motion are the solutions of the equation $F(y) = H$, that is

$$\frac{y^2}{2} - \frac{y_0^2}{2} + \Lambda \ln\left(\frac{1 - y}{1 - y_0}\right) - \frac{(y_0')^2}{2} = 0 \tag{28}$$

which may be solved either numerically or graphically. This means that the trajectory of a PASB is bounded as long as Eq. (2) holds.

Note that the condition (3) is equivalent to

$$y \geq \bar{y} \triangleq 1 - \frac{\tilde{k}}{\tilde{\mu}\,(1 - \tilde{\mu})} < 1 \tag{29}$$

The previous trajectory analysis is therefore valid when $y < \bar{y}$, that is, when $\beta > 0$. Moreover, the constraint on the maximum allowable value of y involves a constraint on $F_{\max}$, that is, on the constant H. As a matter of fact, $y < \bar{y}$ implies

$$H < \bar{H} \triangleq \frac{1}{2}\left[1 - \frac{\tilde{k}}{\tilde{\mu}\,(1 - \tilde{\mu})}\right]^2 + \Lambda \ln\left[\frac{\tilde{k}}{\tilde{\mu}\,(1 - \tilde{\mu})}\right] \tag{30}$$
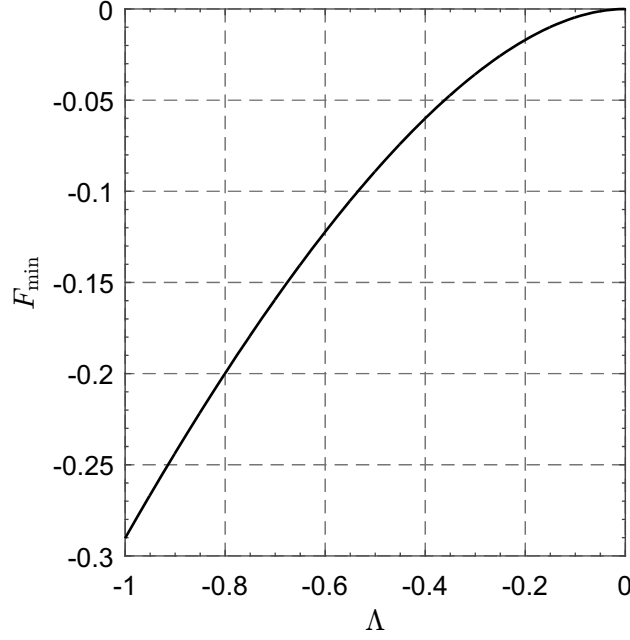
10

Figure 6: Variation of $F_{\min}$ with Λ.

In other terms, if the initial conditions and the physical properties of the PASB are such that $H \geq \bar{H}$, then the thrust model is no longer valid as it would predict negative values of β.

3. Analytical approximation of heliocentric trajectory

The transformation of the PASB dynamics into an equivalent nonlinear oscillator allows an accurate approximation of its heliocentric trajectory to be obtained. This is made possible by paralleling the procedure suggested by Nayfeh and Mook [27], that is, by substituting $y = y_C + \delta y$ into the first of Eqs. (13) and expanding the resulting equation in a Taylor series about $\delta y = 0$. The resulting approximate solution is

$$y \simeq \hat{y} \triangleq y_C + A \cos\left(f\,\theta + B\right) - \frac{A^2\,\alpha_2}{2\,\alpha_1}\left[1 - \frac{\cos\left(2\,f\,\theta + 2\,B\right)}{3}\right] \tag{31}$$

where y_C is given by Eq. (26), while f is the (approximate) natural frequency of the equivalent nonlinear oscillator, that is

$$f \triangleq \sqrt{\alpha_1}\left(1 + A^2\frac{3\,A^2\,\alpha_3}{8\,\alpha_1} - \frac{5\,A^2\,\alpha_2^2}{12\,\alpha_1^2}\right) \tag{32}$$

with $\{\alpha_1, \alpha_2, \alpha_3\}$ defined as

$$\alpha_1 \triangleq 1 - \frac{\Lambda}{\left(1 - y_C\right)^2} \quad,\quad \alpha_2 \triangleq -\frac{\Lambda}{\left(1 - y_C\right)^3} \quad,\quad \alpha_3 \triangleq -\frac{\Lambda}{\left(1 - y_C\right)^4} \tag{33}$$

Since $\Lambda < 0$ and $y_C < 0$, the coefficients α_1, α_2, and α_3 are all strictly positive. The constants A and B must be determined from the initial conditions (the last two of Eqs. (13)) by numerically solving the following system of nonlinear equations

$$\begin{cases} 1 - y_C - \dfrac{1 + e_0\,\cos\nu_0}{\tilde{\mu}} - A\,\cos B + \dfrac{A^2\,\alpha_2}{2\,\alpha_1}\left[1 - \dfrac{\cos\left(2\,B\right)}{3}\right] = 0 & (34) \\[4mm] \dfrac{e_0\,\sin\nu_0}{\tilde{\mu}} + A\,f\,\sin B + \dfrac{A^2\,\alpha_2}{3\,\alpha_1}\,\sin\left(2\,B\right) = 0 & (35) \end{cases}$$

11

where we point out that the constant A is also implicitly contained in f; see Eq. (32). Figure 7 shows the variation of f with $k\,r_{\oplus}$ when $r_0 = r_{\oplus}$, $e_0 = 0$, and $\beta_{\oplus} = 0.1$. It can be seen that the natural frequency of the equivalent nonlinear oscillator is close to unity, which corresponds to when the PASB behaves like a Sun-facing solar sail; see Eq. (15).
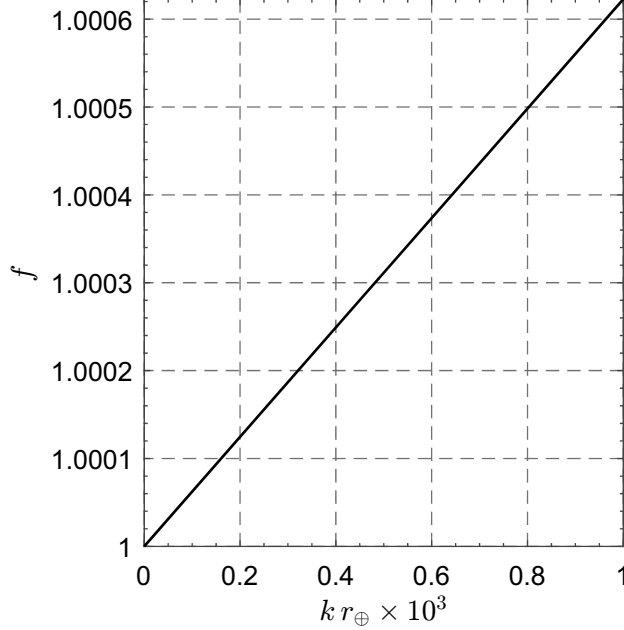

Figure 7: Variation of f with $k\,r_{\oplus}$ when $r_0 = r_{\oplus}$, $e_0 = 0$, and $\beta_{\oplus} = 0.1$.

When A and B have been numerically found from Eqs. (34)-(35), the (approximate) polar form of the heliocentric trajectory is obtained from Eqs. (8)-(12), viz.

$$r \simeq \hat{r} \triangleq \frac{p_0/\tilde{\mu}}{1 - \hat{y}} \equiv \frac{p_0/\tilde{\mu}}{1 - y_C - A\,\cos\left(f\,\theta + B\right) + \dfrac{A^2\,\alpha_2}{2\,\alpha_1}\left[1 - \dfrac{\cos\left(2\,f\,\theta + 2\,B\right)}{3}\right]} \tag{36}$$

This last equation allows the velocity components of the PASB to be written as a function of θ. In fact, bearing in mind the first of Eqs. (9) and Eq. (12), the radial (u) and transverse ($r\,\dot{\theta}$) components of the spacecraft velocity are

$$u = \frac{\sqrt{\mu_{\odot}\,p_0}\,r'}{r^2} \quad , \quad r\,\dot{\theta} = \frac{\sqrt{\mu_{\odot}\,p_0}}{r} \tag{37}$$

where

$$r' \simeq \hat{r}' \triangleq \frac{p_0\,y'}{\tilde{\mu}\,(1 - y)^2} \equiv \frac{-p_0\,f\left[A\,\sin\left(f\,\theta + B\right) + \dfrac{A^2\,\alpha_2}{3\,\alpha_1}\,\sin\left(2\,f\,\theta + 2\,B\right)\right]}{\tilde{\mu}\left\{1 - y_C - A\,\cos\left(f\,\theta + B\right) + \dfrac{A^2\,\alpha_2}{2\,\alpha_1}\left[1 - \dfrac{\cos\left(2\,f\,\theta + 2\,B\right)}{3}\right]\right\}^2} \tag{38}$$

Finally, the approximate expression of time, referred to as $\hat{t}$, may be obtained as a function of θ by evaluating the integral

$$t \simeq \hat{t} \triangleq \frac{1}{\tilde{\mu}^2}\sqrt{\frac{p_0^3}{\mu_{\odot}}}\int_0^{\theta}\left\{1 - y_C - A\,\cos\left(f\,\xi + B\right) + \frac{A^2\,\alpha_2}{2\,\alpha_1}\left[1 - \frac{\cos\left(2\,f\,\xi + 2\,B\right)}{3}\right]\right\}^{-2}\mathrm{d}\xi \tag{39}$$

12

3.1. Case of circular parking orbit

In the special case of a circular parking orbit, the pair $\{A, B\}$ can be analytically calculated as in Ref. [30], where the solutions reported in Ref. [29] are applied to study the phasing maneuvers of a Sun-facing E-sail orbiting around the Sun. More precisely, if $e_0 = 0$, Eq. (35) is solved with $B = 0$, whereas Eq. (34) does not contain f, which in turn depends on A. Substituting $B = 0$ into Eq. (34) we get

$$A = \frac{3\,\alpha_1}{2\,\alpha_2} - \sqrt{\frac{9\,\alpha_1^2}{4\,\alpha_2^2} - \frac{3\,\alpha_1}{\alpha_2}\left(1 - y_C - \frac{1}{\tilde{\mu}}\right)} \tag{40}$$

Since $y_0' = 0$, Eq. (28) gives the extreme values of y as the solutions of the following equation

$$\frac{y^2}{2} - \frac{y_0^2}{2} + \Lambda \ln\left(\frac{1-y}{1-y_0}\right) = 0 \tag{41}$$

which is solved for

$$y = y_0 \quad , \quad y \simeq y_C - A - \frac{A^2\,\alpha_2}{3\,\alpha_1} > y_0 \tag{42}$$

where the upper bound is obtained by calculating the maximum of Eq. (31) with $B = 0$. To summarize, when the parking orbit is circular, the heliocentric trajectory of a PASB is bounded within an annular region, that is, $r \in [r_{\min}, r_{\max}]$, where

$$r_{\min} = r_0 \quad , \quad r_{\max} = \frac{r_0/\tilde{\mu}}{1 - y_C + A + \dfrac{A^2\,\alpha_2}{3\,\alpha_1}} \tag{43}$$

Figure 8 shows the variation of $r_{\max}/r_0$ as a function of $k\,r_\oplus$ and r_0 when $\beta = 0.1$. It is worth noting that the value of $r_{\max}/r_0$ is independent of r_0 when $k = 0$. Moreover, it is easy to verify that, when $k = 0$, $r_{\max}/r_0 = 1/(1 - 2\,\beta_\oplus)$. This occurs because $k = 0$ implies $\tilde{\mu} = (1 - \beta_\oplus)$, $y_C = 0$, $\alpha_1 = 1$, $\alpha_2 = 0$, and $A = \beta_\oplus/(\beta_\oplus - 1)$; compare Eq. (15) with $e_0 = 0$ and Eq. (31) with $f = 1$ and $B = 0$.
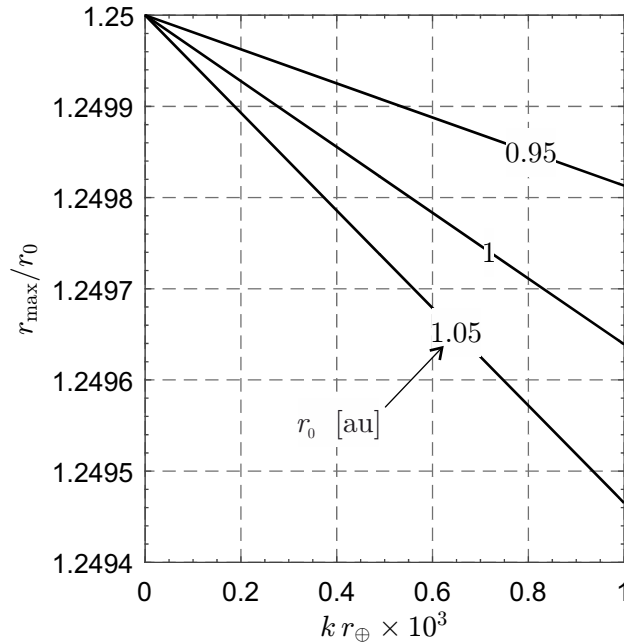

Figure 8: Variation of $r_{\max}/r_0$ as a function of $k\,r_\oplus$ and r_0 when $\beta = 0.1$.

3.2. Simplified trajectory equation

A substantial simplification of the approximate trajectory of a PASB can be obtained by observing that α_2/α_1 and α_3/α_1 are typically much smaller than unity. In fact, they may be written as a function of Λ as

$$\frac{\alpha_2}{\alpha_1} = \frac{\Lambda}{\left(\frac{1}{2} + \sqrt{\frac{1}{4} - \Lambda}\right)\left(2\,\Lambda - \frac{1}{2} - \sqrt{\frac{1}{4} - \Lambda}\right)} \tag{44}$$

$$\frac{\alpha_3}{\alpha_1} = \frac{\Lambda}{\left(\frac{1}{2} + \sqrt{\frac{1}{4} - \Lambda}\right)^2\left(2\,\Lambda - \frac{1}{2} - \sqrt{\frac{1}{4} - \Lambda}\right)} \tag{45}$$

which are plotted in Fig. 9 for $\Lambda \in [-10,\, 0]$.

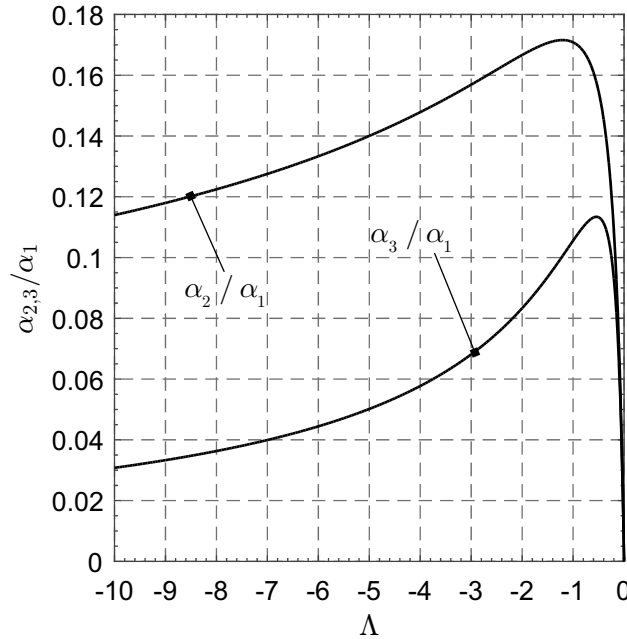

Figure 9: Variation of ratios α_2/α_1 and α_3/α_1 as a function of Λ.

According to Fig. 9, the ratio α_2/α_1 (or α_3/α_1) has a global maximum when $\Lambda \simeq -1.2071$ (or $\Lambda \simeq -0.5428$) and its corresponding value is approximately equal to 0.1716 (or 0.1134). However, since $|\Lambda| \ll 1$, then $\{\alpha_2/\alpha_1,\, \alpha_3/\alpha_1\} \simeq -\Lambda$ and the term $A^2\,\alpha_2/(2\,\alpha_1)$ in Eq. (31) may be neglected, while the natural frequency of the equivalent nonlinear oscillator (see Eq. (32)) can be simplified as

$$f \simeq \sqrt{\alpha_1} \equiv \sqrt{1 - \frac{4\,\Lambda}{\left(1 + \sqrt{1 - 4\,\Lambda}\right)^2}} \tag{46}$$

which is an explicit function of Λ. Neglecting the term $A^2\,\alpha_2/(2\,\alpha_1)$ in Eq. (31) allows Eqs. (36)-(38) to be rewritten in a more compact form as

$$\hat{r} \simeq \frac{p_0/\tilde{\mu}}{1 - y_C - A\,\cos\left(f\,\theta + B\right)} \quad , \quad \hat{r}' \simeq \frac{-p_0\,f\,A\,\sin\left(f\,\theta + B\right)}{\tilde{\mu}\,\left[1 - y_C - A\,\cos\left(f\,\theta + B\right)\right]^2} \tag{47}$$

from which the extremes of the Sun-spacecraft distance are given by

$$r_{\min} = \min\left(\frac{p_0/\tilde{\mu}}{1 - y_C \pm A}\right) \quad , \quad r_{\max} = \max\left(\frac{p_0/\tilde{\mu}}{1 - y_C \pm A}\right) \tag{48}$$

14

In this case, the computation of the integral in Eq. (39) is remarkably simplified. In fact, neglecting the term $A^2 \alpha_2/(2 \alpha_1)$, the antiderivative of the integrating function in Eq. (39) is

$$G(\theta) = \frac{2 A g}{f \left[A^2 - (y_C - 1)^2\right] \left[(y_C - A - 1) g^2 + A + y_C - 1\right]} +$$

$$+ \frac{2 (y_C - 1) \arctan\left(-g \sqrt{\dfrac{y_C - A - 1}{y_C + A - 1}}\right)}{f \left[(y_C - 1)^2 - A^2\right]^{3/2}} \quad (49)$$

where

$$g = g(\theta) \triangleq \tan\left(\frac{f \theta + B}{2}\right) \quad (50)$$

Therefore, the flight time may be approximated as

$$t \simeq \hat{t} \triangleq \sqrt{\frac{p_0^3}{\mu_\odot}} \frac{G(\theta) - G(0)}{\tilde{\mu}^2} \quad (51)$$

3.3. Orbital parameters of osculating orbit

Consider now the evolution of the orbital parameters of the osculating orbit, that is, the evolution of semi-major axis and eccentricity and the rotation of the apse line. The osculating semi-major axis may be obtained from the equation of the specific mechanical energy $\mathcal{E}$ as

$$a \triangleq -\frac{\mu_\odot}{2 \mathcal{E}} \quad (52)$$

where

$$\mathcal{E} \triangleq \frac{u^2 + (r \dot{\theta})^2}{2} - \frac{\mu_\odot}{r} = \frac{\mu_\odot}{r} \left\{ \frac{p_0}{2 r} \left[1 + \left(\frac{r'}{r}\right)^2\right] - 1 \right\} \quad (53)$$

from which its approximate expression is

$$a \simeq \hat{a} \triangleq \frac{\hat{r}^4}{2 \hat{r}^3 - p_0 \left[\hat{r}^2 + (\hat{r}')^2\right]} \quad (54)$$

where $\hat{r}$ and $\hat{r}'$ are given by Eqs. (36)-(38), respectively, or by Eqs. (47) when $A^2 \alpha_2/(2 \alpha_1)$ is neglected. The eccentricity of the osculating orbit is accurately approximated as

$$e \simeq \hat{e} \triangleq \sqrt{1 - \frac{p_0}{\hat{a}}} = \frac{\sqrt{\hat{r}^4 - 2 p_0 \hat{r}^3 + p_0^2 \left[\hat{r}^2 + (\hat{r}')^2\right]}}{\hat{r}^2} \quad (55)$$

Finally, the rotation $\Delta\omega$ of the apse line corresponds to the rotation of the eccentricity vector $\boldsymbol{e}$. The components of the eccentricity vector in an inertial reference frame $\mathcal{T}_I$ may be approximated as

$$[\boldsymbol{e}]_{\mathcal{T}_I} \simeq [\hat{\boldsymbol{e}}]_{\mathcal{T}_I} \triangleq \frac{p_0}{\hat{r}} \begin{bmatrix} (\hat{r}'/\hat{r}) \sin\theta + \cos\theta \\ \sin\theta - (\hat{r}'/\hat{r}) \cos\theta \\ 0 \end{bmatrix} \quad (56)$$

from which

$$\Delta\omega \simeq \Delta\hat{\omega} \triangleq \mathrm{arctan2}\left[\sin\theta - (\hat{r}'/\hat{r}) \cos\theta, \, (\hat{r}'/\hat{r}) \sin\theta + \cos\theta\right] \quad (57)$$

Note that, since the functions $\hat{r}$ and $\hat{r}'$ are periodic with respect to θ with a period $\Theta = 2 \pi/f$, the variations of $\hat{a}$, $\hat{e}$, and $\Delta\hat{\omega}$ are also periodic with respect to θ with the same period.

4. Model validation

This section discusses the validation of the analytical approximation of the heliocentric trajectory, both in its complete form of Eq. (36) and in the simplified one obtained by neglecting $A^2 \alpha_2/(2\alpha_1)$; see the first of Eqs. (47). Such a validation is performed by comparing the approximate results with those obtained by numerically integrating Eqs. (13) with a variable order Adams-Bashforth-Moulton PECE solver [43] with absolute and relative errors equal to 10^{-12}.

The accuracy of the analytical approximation is measured by the relative error in orbital radius, that is, by evaluating the function $\epsilon_r = \epsilon_r(\theta)$, defined as

$$\epsilon_r \triangleq \frac{|r - \hat{r}|}{r} \tag{58}$$

where r (or $\hat{r}$) is the value of the Sun-spacecraft distance at a given θ evaluated through the numerical integration of the equations of motion (or using the approximate model). Note that r and $\hat{r}$ are calculated with the same initial conditions (e_0, p_0, and ν_0) and the same performance parameters ($\beta_\oplus$ and k) of the PASB.

Figure 10 shows the maximum value of $\epsilon_r(\theta)$ as a function of ν_0 during 10 revolutions around the Sun (i.e., for $\theta/\Theta \in [0, 10]$), when $e_0 = e_\oplus \triangleq 0.0167086$, $p_0 = r_\oplus (1 - e_\oplus^2)$, $\beta_\oplus = 0.1$, and $k r_\oplus = 10^{-3}$. Such a situation corresponds to a deployment of the PASB on a parabolic escape orbit relative to the Earth. In particular, Fig. 10(a) shows $\max(\epsilon_r)$ when r is calculated through Eq. (36), whereas Fig. 10(b) shows $\max(\epsilon_r)$ when r is given by the first of Eqs. (47). In both cases the maximum relative error is very small as it never exceeds 1.6×10^{-5}.

Figure 11 shows the maximum relative error during 10 revolutions around the Sun, when $e_0 = 0$ and $p_0 = r_\oplus$, as a function of $\beta_\oplus \in [0, 0.1]$ and $k r_\oplus = \{10^{-4}, 2 \times 10^{-4}, 5 \times 10^{-4}, 10^{-3}\}$. Although $\max(\epsilon_r)$ increases with $\beta_\oplus$ and $k r_\oplus$, it never exceeds 1.2×10^{-5}. In conclusion, Figs. 10-11 confirm that the approximation given by the fist of Eqs. (47) is very accurate.

Finally, the accuracy of the estimate of t, obtained from Eq. (51), has been investigated by numerically solving the differential equation

$$t' = \frac{\sqrt{p_0^3/\mu_\odot}}{\tilde{\mu}^2 (1 - y)^2} \tag{59}$$

In this case, the relative error in terms of flight time $\epsilon_t = \epsilon_t(\theta)$ is defined for $t > 0$ as

$$\epsilon_t \triangleq \frac{|t - \hat{t}|}{t} \tag{60}$$

Figure 12 shows the function $\epsilon_t = \epsilon_t(\theta)$ for $\theta/\Theta \in (0, 10]$ when $e_0 = e_\oplus$, $p_0 = r_\oplus (1 - e_\oplus^2)$, $\nu_0 = 90 \deg$, $\beta_\oplus = 0.1$, and $k r_\oplus = 10^{-3}$. Note that ϵ_t never exceeds 1.7×10^{-5}.

Figure 13 shows the parking orbit and the propelled trajectory when $p_0 = r_\oplus (1 - e_\oplus^2)$, $e_0 = e_\oplus$, $\nu_0 = 90 \deg$, $\beta_\oplus = 0.1$, and $k r_\oplus = 10^{-3}$. The numerical solution is plotted with a solid black line, while the approximate one is drawn with a dotted red line. Notably, the two trajectories are substantially coincident.

5. Mission applications

Since the propulsive acceleration model described by Eqs. (1)-(2) is valid when $r \simeq r_\oplus$ [16], the choice of the mission scenarios must necessarily consider the limits of applicability of the thrust model itself. In particular, we will assume that the parking orbit is nearly circular (i.e., $e_0 \ll 1$), $r_0 \simeq r_\oplus$, and $\beta_\oplus \ll 1$. These hypotheses guarantee that $r \simeq r_\oplus$ for all $t \geq t_0$.

To simplify the following analysis, we will also consider the simplified case in which the heliocentric trajectory is given by Eq. (47). Two mission applications are studied, that is, the execution of a phasing maneuver on an elliptical working orbit and the rotation of the apse line of the osculating orbit. It is worth noting that the possible applications of a PASB are limited by the fact that a solar balloon can only generate a purely radial thrust. However, unlike a solar sail, no attitude correction maneuver is necessary since the balloon generates a radial thrust whatever its orientation is. Nonetheless, the analyzed mission
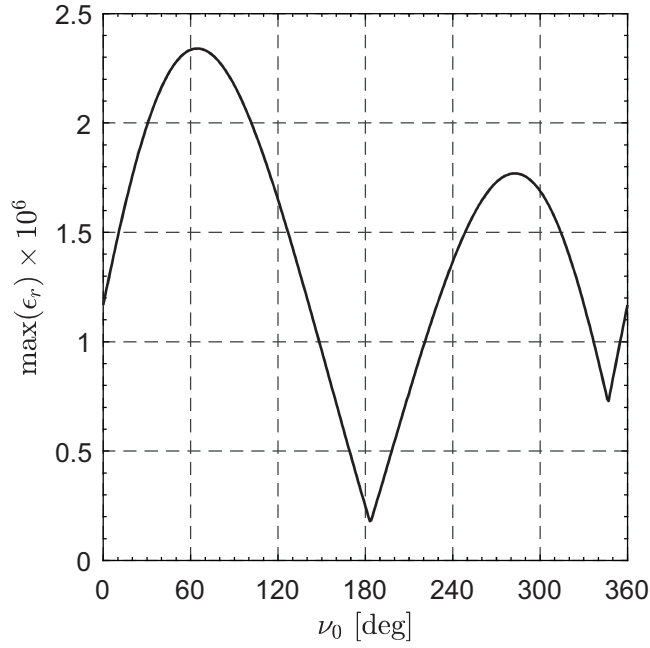
(a) $A_2\,\alpha_2/(2\,\alpha_1) \neq 0$.
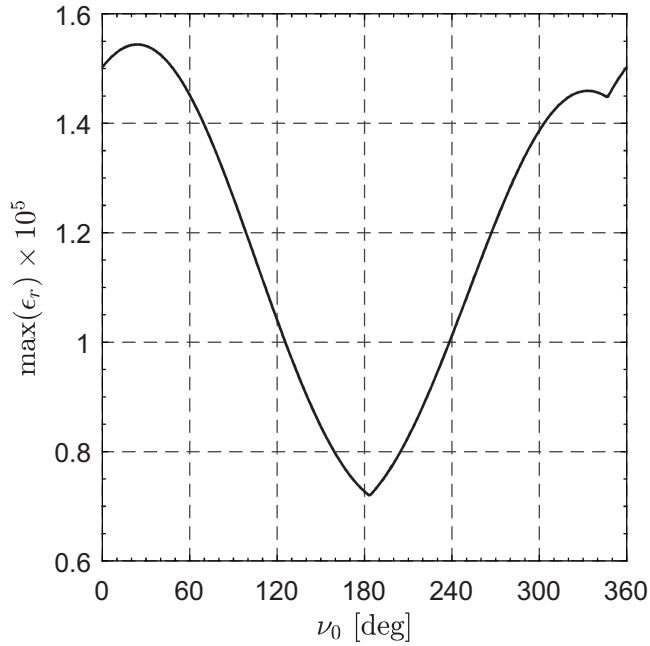
(b) $A_2\,\alpha_2/(2\,\alpha_1) = 0$.

Figure 10: Maximum relative error in orbital radius during 10 revolutions around the Sun, when $e_0 = e_\oplus$, $p_0 = r_\oplus\,(1 - e_\oplus^2)$, $\beta_\oplus = 0.1$, and $k\,r_\oplus = 10^{-3}$, as a function of ν_0.

scenarios are useful for several practical purposes. A phasing maneuver might be useful, for example, when its aim is to place a spacecraft in the L_4 or L_5 Lagrangian point of the Sun-[Earth+Moon] system for the exploration of the Trojan asteroids [44]. An artificial precession of the apse line might instead be useful for the generation of Earth-following orbits, which are practical for solar activity monitoring and near-Earth
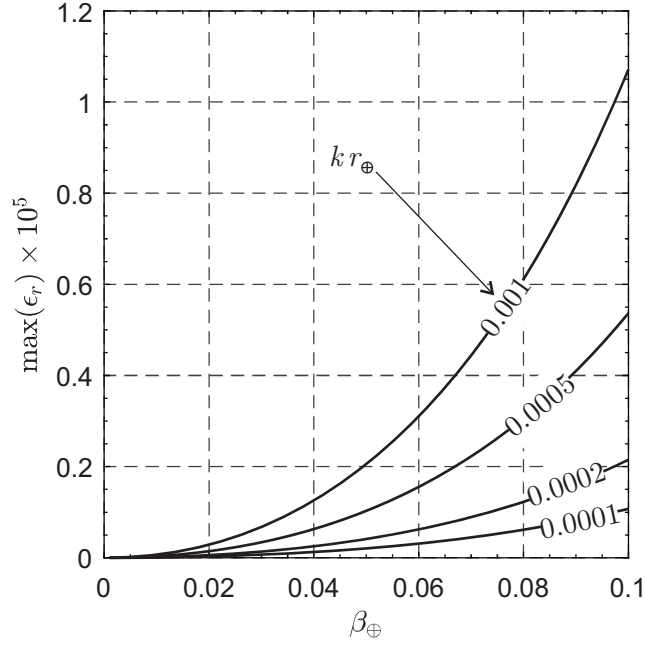
17

Figure 11: Maximum relative error in orbital radius during 10 revolutions around the Sun, when $p_0 = r_\oplus$ and $e_0 = 0$, as a function of $\beta_\oplus$ and $k\, r_\oplus$.
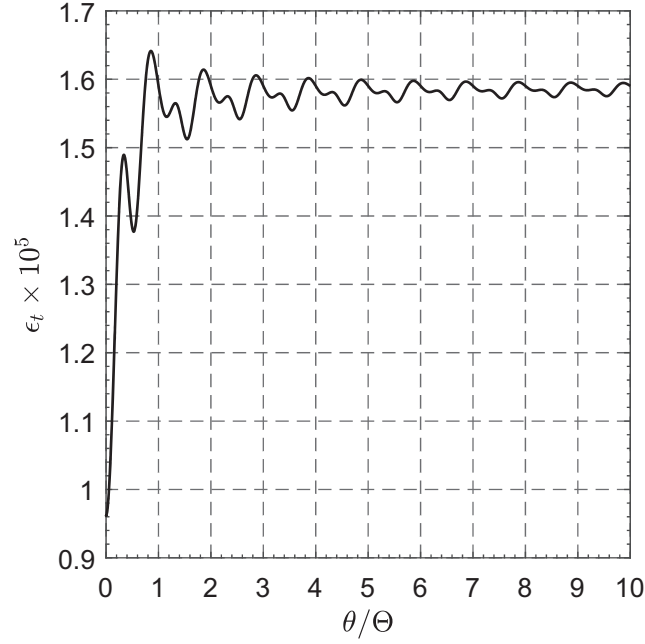

Figure 12: Evolution of the relative error in time, when $e_0 = e_\oplus$, $p_0 = r_\oplus\,(1 - e_\oplus^2)$, $\nu_0 = 90\,\mathrm{deg}$, $\beta_\oplus = 0.1$, and $k\, r_\oplus = 10^{-3}$, as a function of $\theta/\Theta \in (0, 10]$.

object surveillance [45, 46].

5.1. Phasing maneuvers

A phasing maneuver consists in changing the angular position of a spacecraft along an elliptical working orbit in such a way that, at the end of the maneuver, the spacecraft true anomaly is different from the one
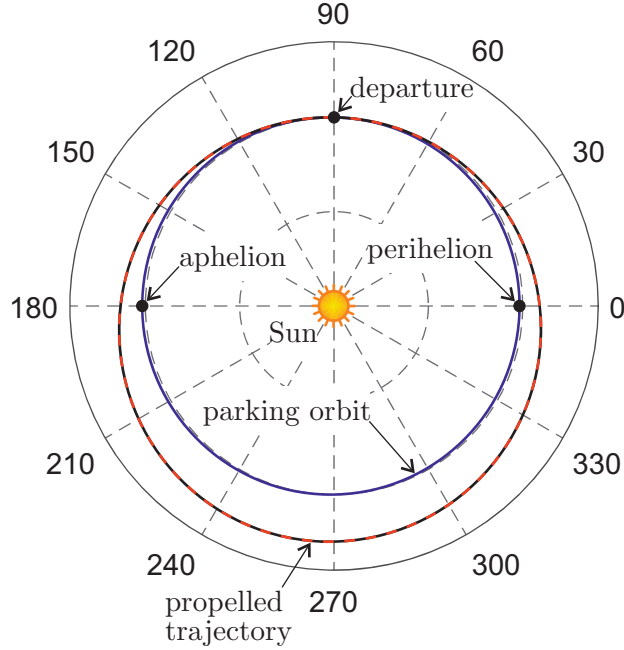
Figure 13: Numerical (solid black line) and approximate (dotted red line) trajectories when $p_0 = r_\oplus (1 - e_\oplus^2)$, $e_0 = e_\oplus$, $\nu_0 = 90 \deg$, $\beta_\oplus = 0.1$, and $k \, r_\oplus = 10^{-3}$, as a function of $\theta/\Theta \in [0, 10]$.

it would have as a result of the gravitational action of the primary body alone. The use of a propellantless propulsion system is a convenient way of performing such a mission. Suffice it to mention the work by McInnes [47], who investigated the azimuthal repositioning of payloads in a heliocentric circular orbit using a solar sail, or the paper by Bassetto et al. [35], who analyzed the phasing maneuver of a solar sail along an elliptical heliocentric orbit, where the phasing orbit is composed of two symmetric logarithmic spiral trajectories connected with a single coasting arc. The same problem was also addressed in an optimal framework in Ref. [48], where the spacecraft primary propulsion system is a solar sail, and in Refs. [49, 50], where the spacecraft is propelled by an E-sail. In terms of control law, the simplest way to perform a phasing maneuver is to accomplish it by applying a purely radial thrust, as illustrated in Ref. [30] in the case of a spacecraft equipped with a Sun-facing E-sail.

Typically, a phasing maneuver is designed by first selecting the phasing angle and then by determining the required thrust profile and flight time. In our case, the aim is to find the relationships among $\beta_\oplus$, k, p_0, the duration t_f of the phasing maneuver, and the phasing angle ϕ. Here, t_f corresponds to the length of propelled trajectory and coincides with the minimum time interval that the PASB takes to come back to the initial orbit after t_0. The initial orbit is restored when $a = a_0$, $e = e_0$, and $\Delta\omega = 0$. Therefore, t_f may be approximated with Eq. (51), that is

$$t_f \simeq \sqrt{\frac{p_0^3}{\mu_\odot} \frac{G(\Theta) - G(0)}{\tilde{\mu}^2}} \tag{61}$$

where

$$\Theta \simeq \frac{2\pi}{\sqrt{\alpha_1}} \equiv \frac{2\pi}{\sqrt{1 - \dfrac{4\Lambda}{\left(1 + \sqrt{1 - 4\Lambda}\right)^2}}} \tag{62}$$

depends on Λ, that is, on $\{\beta_\oplus, k, p_0\}$. The corresponding phasing angle ϕ is given, as an implicit function of $\{\beta_\oplus, k, p_0, e_0, \nu_0\}$, by

$$\phi \simeq \Theta - (\nu_f - \nu_0) \tag{63}$$

19

where ν_f is the solution of an inverse Kepler's problem, that is

$$\sqrt{\frac{a_0^3}{\mu_\odot}} \left(E_f - e_0 \sin E_f - E_0 + e_0 \sin E_0 \right) - t_f = 0 \tag{64}$$

where

$$E_0 \triangleq 2 \arctan\left[\sqrt{\frac{1 - e_0}{1 + e_0}} \tan\left(\frac{\nu_0}{2}\right) \right] \quad , \quad E_f \triangleq 2 \arctan\left[\sqrt{\frac{1 - e_0}{1 + e_0}} \tan\left(\frac{\nu_f}{2}\right) \right] \tag{65}$$

are the eccentric anomalies at the initial time and at the end of the phasing maneuver, respectively. Note that the difference $(\nu_f - \nu_0)$ must range within the interval $[0, 2\pi)$ rad. Finally, it is worth noting that the flight time and the corresponding phasing angle are obtained assuming a single period of the equivalent nonlinear oscillator. However, multiple phasing angles may also be achieved by simply considering two or more periods of the equivalent oscillator.

5.2. Precession of the line of apsides

According to Eq. (57), the effect of the propulsive acceleration produced by a PASB determines a rotation of the apse line of the osculating orbit. Note that Eqs. (6) do not take into account perturbative forces that, through a little change in the spacecraft states, may cause a rotation of the apse line of the osculating orbit. For this reason, the only force capable of rotating the apse line of the osculating orbit is the propulsive one generated by the solar balloon. Since the propulsive acceleration cannot be set to zero, a rotation of the apse line of the osculating orbit requires the balloon to be released at the end of the maneuver. In particular, it is interesting to evaluate the apse rotation when, after a leg of propelled trajectory, the initial values of semilatus rectum and eccentricity are restored. Over one period of propelled trajectory this obviously occurs when $\theta = \{0, \Theta\}$, that is, at the initial time or at the end of the propelled arc, but these are not the only possible cases. In fact, assuming $\{e_0, \nu_0\} \neq 0$, there is a value of θ (that is, $\theta^\star \in (0, \Theta)$) such that the corresponding values of p, e, and r are equal to the initial ones and, at the same time, $\Delta\omega \neq 0$.

It can be verified that, when $\theta = \theta^\star$, then $r'(\theta^\star) = -r'(0) = -r'(\Theta)$. With reference to the first of Eqs. (47), the approximate value of $\theta^\star$ (i.e., $\hat{\theta}^\star$) must satisfy the following equality

$$A \cos\left(f\,\hat{\theta}^\star + B \right) = 1 - y_C - \frac{1 + e_0 \cos\nu_0}{\tilde{\mu}} \tag{66}$$

In general, Eq. (66) admits two solutions, that is

$$\hat{\theta}_1^\star = \frac{1}{f} \left\{ \arccos\left[\frac{1}{A} \left(1 - y_C - \frac{1 + e_0 \cos\nu_0}{\tilde{\mu}} \right) \right] - B \right\} \tag{67}$$

$$\hat{\theta}_2^\star = \frac{1}{f} \left\{ 2\pi - \arccos\left[\frac{1}{A} \left(1 - y_C - \frac{1 + e_0 \cos\nu_0}{\tilde{\mu}} \right) \right] - B \right\} \tag{68}$$

which give real values if

$$-1 \leq \frac{1}{A} \left(1 - y_C - \frac{1 + e_0 \cos\nu_0}{\tilde{\mu}} \right) \leq 1 \tag{69}$$

In fact, the use of the approximate relation (66) makes the solutions (67)-(68) complex for certain combinations of e_0 and ν_0. When the inequality (69) is not met, the solutions (67)-(68) cannot be used, and an estimate of $\theta^\star$ must be obtained numerically. However, Eqs. (67)-(68) give complex numbers in the proximity of the perihelion or aphelion of the parking orbit, that is, when $\nu_0 \simeq \{0, 180\}$ deg. If, instead, the condition (69) is satisfied, the choice of the right value of $\theta^\star$ must be made according to the following scheme

$$\hat{\theta}^\star = \begin{cases} \min\left(\hat{\theta}_1^\star, \hat{\theta}_2^\star \right) & \text{if} \quad \sin\nu_0 > 0 \\[2mm] \max\left(\hat{\theta}_1^\star, \hat{\theta}_2^\star \right) & \text{if} \quad \sin\nu_0 < 0 \end{cases} \tag{70}$$

For example, Fig. 14 shows the variation of $\hat{\theta}^\star$ as a function of ν_0 when $a_0 = r_\oplus$, $e_0 = \{e_\oplus, 2\,e_\oplus, 3\,e_\oplus\}$, $\beta_\oplus = 0.1$, and $k\,r_\oplus = 10^{-3}$. Figure 15 illustrates the corresponding (approximate) precession of the line of apsides, which is obtained by substituting $\hat{\theta}^\star$ into Eq. (57). By way of example, a precession of -90 deg of the line of apsides is obtained with a swept angle of about 19 deg and starting from $\nu_0 \simeq 251$ deg.
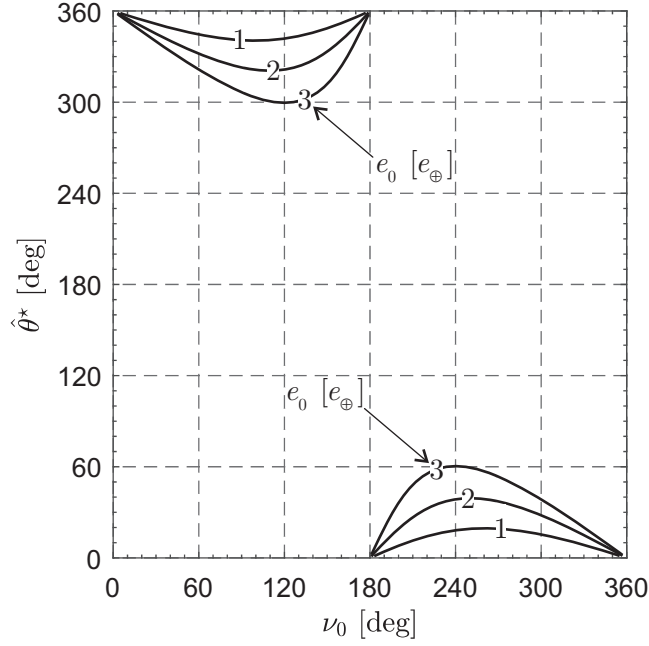
Figure 14: Variation of $\hat{\theta}^\star$ with ν_0 when $a_0 = r_\oplus$, $e_0 = \{e_\oplus, 2\,e_\oplus, 3\,e_\oplus\}$, $\beta_\oplus = 0.1$, and $k\,r_\oplus = 10^{-3}$.
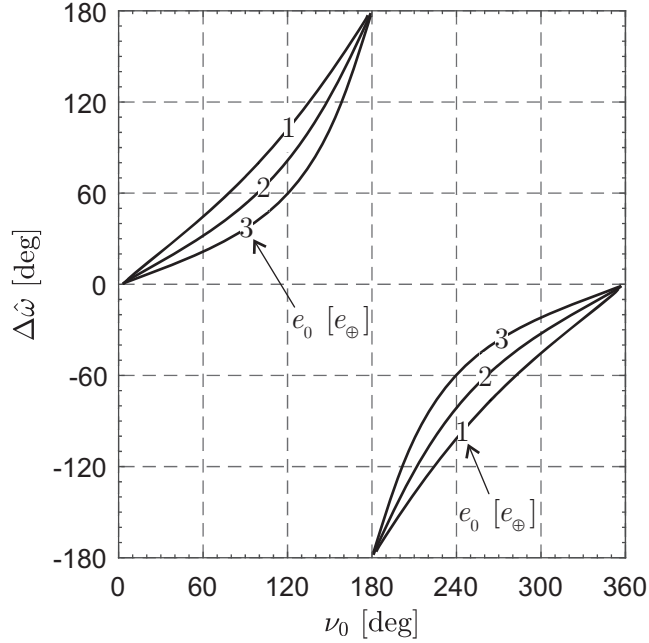

Figure 15: Variation of $\Delta\hat{\omega}$ with ν_0 when $a_0 = r_\oplus$, $e_0 = \{e_\oplus, 2\,e_\oplus, 3\,e_\oplus\}$, $\beta_\oplus = 0.1$, and $k\,r_\oplus = 10^{-3}$.

6. Conclusions

This paper has analyzed the heliocentric motion of a passively actuated solar balloon placed at a distance of about one astronomical unit from the Sun. The heliocentric trajectory has been found by exploiting the possibility of reducing the spacecraft two-dimensional dynamics to an equivalent nonlinear oscillator with a single degree of freedom. The approximate solution available for such a nonlinear oscillator is able to

21

accurately describe the motion of the passively actuated solar balloon. Finally, two mission scenarios of practical interest have been discussed with the aid of the approximate model.

The simplified mathematical model allows the designer to explore a large number of passively actuated solar balloon-based mission scenarios with a negligible computational cost and an accuracy consistent with a preliminary mission phase. The main drawback of the proposed set of analytical expressions is related to the intrinsic limits of the employed thrust model. In this sense, a natural extension of this work is to look for a more refined thrust model, capable of describing the passively actuated solar balloon dynamics even when the distance from the Sun deviates significantly from one astronomical unit. A further improvement of the analysis is to evaluate the performance of an active β-control.

References

[1] I. I. Shapiro, H. M. Jones, Perturbations of the orbit of the Echo balloon, Science 132 (3438) (1960) 1484–1486, doi: 10.1126/science.132.3438.1484.

[2] D. O. Muhleman, R. H. Hudson, D. B. Holdridge, R. L. Carpenter, K. C. Oslund, Observed solar pressure perturbations of Echo I, Science 132 (3438) (1960) 1487, doi: 10.1126/science.132.3438.1487.

[3] A. G. Buckingham, Y. C. Lim, J. A. Miller, Orbit position control using solar pressure, Journal of Spacecraft and Rockets 2 (6) (1965) 863–867, doi: 10.2514/3.28305.

[4] A. F. Heaton, A. T. Brinckerhoff, Solar sail model validation from Echo trajectories, in: Proceedings of the AAS/AIAA 17th Space Flight Mechanics Meetings, Sedona, Arizona, January 28 - February 1, 2007, paper AAS 07-124.

[5] G. Vulpetti, S. Scaglione, Aurora project: estimation of the optical sail parameters, Acta Astronautica 44 (2) (1999) 123–132, doi: 10.1016/S0094-5765(99)00038-7.

[6] S. Scaglione, G. Vulpetti, Aurora project: removal of plastic substrate to obtain an all-metal solar sail, Acta Astronautica 44 (2) (1999) 147–150, doi: 10.1016/S0094-5765(99)00041-7.

[7] M. Bassetto, A. A. Quarta, G. Mengali, V. Cipolla, Trajectory analysis of a sun-facing solar sail with optical degradation, Journal of Guidance, Control, and Dynamics 43 (9) (2020) 1727–1732, doi: 10.2514/1.G005214.

[8] T. Pino, C. Circi, G. Vulpetti, Wrinkling analysis for small solar-photon sails: An experimental and analytic approach for trajectory design, Advances in Space Research 63 (11) (2019) 3675–3690, doi: 10.1016/j.asr.2019.02.016.

[9] J. D. Biggs, C. R. McInnes, Passive orbit control for space-based geo-engineering, Journal of Guidance, Control, and Dynamics 33 (3) (2010) 1017–1020, doi: 10.2514/1.46054.

[10] C. Lücking, C. Colombo, C. R. McInnes, Orbit control of high area-to-mass ratio spacecraft using electrochromic coating, in: 61st International Astronautical Congress, Prague, Czech Republic, 2010, paper IAC-10.C1.2.7.

[11] G. Mengali, A. A. Quarta, Heliocentric trajectory analysis of Sun-pointing Smart Dust with electrochromic control, Advances in Space Research 57 (4) (2016) 991–1001, doi: 10.1016/j.asr.2015.12.017.

[12] L. Niccolai, M. Bassetto, A. A. Quarta, G. Mengali, A review of Smart Dust architecture, dynamics, and mission applications, Progress in Aerospace Sciences 106 (2019) 1–14, doi: 10.1016/j.paerosci.2019.01.003.

[13] Y. Takao, O. Mori, M. Matsushita, A. K. Sugihara, Solar electric propulsion by a solar power sail for small spacecraft missions to the outer solar system, Acta Astronautica 181 (2021) 362–376, doi: 10.1016/j.actaastro.2021.01.020.

[14] Y. Chu, S. Firuzi, S. Gong, Controllable liquid crystal diffractive sail and its potential applications, Acta Astronautica 182 (2021) 37–45, doi: 10.1016/j.actaastro.2021.02.003.

[15] G. Vulpetti, C. Circi, T. Pino, Coronal Mass Ejection early-warning mission by solar-photon sailcraft, Acta Astronautica 140 (2017) 113–125, doi: 10.1016/j.actaastro.2017.07.042.

[16] G. Aliasi, G. Mengali, A. A. Quarta, Passive control feasibility of collinear equilibrium points with solar balloons, Journal of Guidance, Control, and Dynamics 35 (5) (2012) 1657–1661, doi: 10.2514/1.57393.

[17] R. Funase, O. Mori, Y. Tsuda, Y. Shirasawa, T. Saiki, Y. Mimasu, J. Kawaguchi, Attitude control of IKAROS solar sail spacecraft and its flight results, in: 61st International Astronautical Congress, Vol. 6, Prague, Czech Republic, 2010, pp. 4720–4725.

[18] R. Funase, J. Kawaguchi, O. Mori, H. Sawada, Y. Tsuda, IKAROS, a solar sail demonstrator and its application to Trojan asteroid exploration, in: 53rd AIAA/ASME/ASCE/AHS/ASC Structural Dynamics and Materials Conference, Honolulu (HI), USA, 2012, AIAA Paper 2012-1748.

[19] Y. Tsuda, O. Mori, R. Funase, H. Sawada, T. Yamamoto, T. Saiki, T. Endo, K. Yonekura, H. Hoshino, J. Kawaguchi, Achievement of IKAROS - Japanese deep space solar sail demonstration mission, Acta Astronautica 82 (2) (2013) 183–188, doi: 10.1016/j.actaastro.2012.03.032.

[20] L. Johnson, M. Whorton, A. Heaton, R. Pinson, G. Laue, C. Adams, NanoSail-D2: A solar sail demonstration mission, Acta Astronautica 68 (5-6) (2011) 571–575, doi: 10.1016/j.actaastro.2010.02.008.

[21] T. Svitek, L. Friedman, W. Nye, C. Biddy, M. Nehrenz, Voyage continues - Lightsail-1 mission by the Planetary Society, in: 61st International Astronautical Congress, Vol. 1, Prague, Czech Republic, 2010, pp. 802–810.

[22] B. Betts, B. Nye, J. Vaughn, E. Greeson, R. Chute, D. Spencer, R. Ridenoure, R. Munakata, S. Wong, A. Diaz, D. Stetson, J. Foley, J. Bellardo, B. Plante, Lightsail 1 mission results and public outreach strategies, in: The 4th International Symposium on Solar Sailing, Kyoto Research Park, Kyoto, Japan, 2017, Paper 17093.

[23] B. Betts, D. A. Spencer, B. Nye, R. Munakata, J. Bellardo, S. Wong, A. Diaz, R. Ridenoure, B. Plante, J. Foley, J. Vaughn, Lightsail 2: Controlled solar sailing using a CubeSat, in: The 4th International Symposium on Solar Sailing, Kyoto Research Park, Kyoto, Japan, 2017, Paper 17053.

[24] G. Aliasi, G. Mengali, A. A. Quarta, Artificial equilibrium points for a solar balloon in the α Centauri system, Acta Astronautica 104 (2) (2014) 464–471, doi: 10.1016/j.actaastro.2014.03.006.

[25] C. A. Burdet, Le mouvement keplerien et les oscillateurs harmoniques, Journal für die reine und angewandte Mathematik 1969 (238) (1969) 71–84, doi: 10.1515/crll.1969.238.71.

[26] J. M. Ferrándiz, A general canonical transformation increasing the number of variables with application to the two-body problem, Celestial Mechanics and Dynamical Astronomy 41 (1-4) (1987) 343–357, doi: 10.1007/BF01238770.

[27] A. H. Nayfeh, D. T. Mook, Nonlinear Oscillations, Wiley Classics Library, New York, 1995, Ch. 2, pp. 67–71.

[28] G. Mengali, A. A. Quarta, G. Aliasi, A graphical approach to electric sail mission design with radial thrust, Acta Astronautica 82 (2) (2013) 197–208, doi: 10.1016/j.actaastro.2012.03.022.

[29] A. A. Quarta, G. Mengali, Analysis of electric sail heliocentric motion under radial thrust, Journal of Guidance, Control, and Dynamics 39 (6) (2016) 1431–1435, doi: 10.2514/1.G001632.

[30] M. Bassetto, L. Boni, G. Mengali, A. A. Quarta, Electric sail phasing maneuvers with radial thrust, Acta Astronautica 179 (2021) 99–104, doi: 10.1016/j.actaastro.2020.10.025.

[31] P. Anderson, M. Macdonald, C. Yen, Novel orbits of Mercury, Venus and Mars enabled using low-thrust propulsion, Acta Astronautica 94 (2) (2014) 634–645, doi: 10.1016/j.actaastro.2013.08.018.

[32] C. Fuglesang, M. G. de Herreros Miciano, Realistic sunshade system at L_1 for global temperature control, Acta Astronautica 186 (8) (2021) 269–279, doi: 10.1016/j.actaastro.2021.04.035.

[33] C. L. Staugaitis, L. Kobren, Mechanical and physical properties of the Echo II metal-polymer laminate, Technical Note (TN) NASA TN D-3409, NASA (August 1966).

[34] J. A. Atchison, M. A. Peck, A passive, Sun-pointing, millimeter-scale solar sail, Acta Astronautica 67 (1–2) (2010) 108–121, doi: 10.1016/j.actaastro.2009.12.008.

[35] M. Bassetto, L. Niccolai, A. A. Quarta, G. Mengali, Logarithmic spiral trajectories generated by solar sails, Celestial Mechanics and Dynamical Astronomy 130 (2) (2018) Article number 18, doi: 10.1007/s10569-017-9812-6.

[36] B. Dachwald, W. Seboldt, M. Macdonald, G. Mengali, A. A. Quarta, C. R. McInnes, L. Rios-Reyes, D. J. Scheeres, B. Wie, M. Görlich, F. Lura, B. Diedrich, V. Baturkin, V. L. Coverstone, M. Leipold, G. P. Garbe, Potential solar sail degradation effects on trajectory and attitude control, in: AIAA Guidance, Navigation, and Control Conference and Exhibit, San Francisco, USA, 2005, paper AIAA 2005-6172.

[37] Z. Serfontein, J. Kingston, S. Hobbs, S. A. Impey, A. I. Aria, I. E. Holbrough, J. C. Beck, Effects of long-term exposure to the low-earth orbit environment on drag augmentation systems, In press. Acta Astronautica doi: 10.1016/j.actaastro.2021.06.009.

[38] T. Fukushima, New two-body regularization, Astronomical Journal 133 (1) (2007) 1–10, doi: 10.1086/509606.

[39] A. A. Quarta, G. Mengali, Linear systems approach to multiple-impulse trajectory analysis via regularization, Journal of Guidance, Control, and Dynamics 33 (5) (2010) 1679–1683, doi: 10.2514/1.50133.

[40] A. A. Quarta, G. Mengali, New look to the constant radial acceleration problem, Journal of Guidance, Control, and Dynamics 35 (3) (2012) 919–929, doi: 10.2514/1.54837.

[41] W. P. Sun, C. W. Lim, B. S. Wu, C. Wang, Analytical approximate solutions to oscillation of a current-carrying wire in a magnetic field, Nonlinear Analysis: Real World Applications 10 (3) (2009) 1882–1890, doi: 10.1016/j.nonrwa.2008.02.028.

[42] S. S. Ganji, A. Barari, A. Fereidoon, S. Karimpour, On the behaviour of current-carrying wire-conductors and bucking of a column, Mechanika 19 (3) (2013) 306–315, doi: 10.5755/j01.mech.19.3.4659.

[43] L. F. Shampine, M. W. Reichelt, The MATLAB ODE suite, SIAM Journal on Scientific Computing 18 (1) (1997) 1–22, doi: 10.1137/S1064827594276424.

[44] O. Trivailo, Spacecraft stability, dynamics and control near the triangular Lagrange points influenced by multiple Trojan asteroids, Acta Astronautica 60 (8-9) (2007) 658–675, doi: 10.1016/j.actaastro.2006.07.015.

[45] J. Heiligers, C. R. McInnes, Solar sail heliocentric earth-following orbits, Journal of Guidance, Control and Dynamics 38 (5) (2015) 937–944, doi: 10.2514/1.G000579.

[46] M. Bassetto, A. A. Quarta, G. Mengali, Locally-optimal electric sail transfer, Proceedings of the Institution of Mechanical Engineers, Part G: Journal of Aerospace Engineering 233 (1) (2019) 166–179, doi: 10.1177/0954410017728975.

[47] C. R. McInnes, Azimuthal repositioning of payloads in heliocentric orbit using solar sails, Journal of Guidance, Control, and Dynamics 26 (4) (2003) 662–664, doi: 10.2514/2.5098.

[48] A. A. Quarta, G. Mengali, Optimal solar sail phasing trajectories for circular orbit, Journal of Guidance, Control, and Dynamics 36 (6) (2013) 1821–1824, doi: 10.2514/1.59372.

[49] G. Mengali, A. A. Quarta, G. Aliasi, Heliocentric phasing performance of electric sail spacecraft, Acta Astronautica 127 (2016) 474–481, doi: 10.1016/j.actaastro.2016.06.033.

[50] L. Niccolai, A. Caruso, A. A. Quarta, G. Mengali, Electric sail phasing maneuvers for constellation deployment, Acta Astronautica 177 (2020) 853–861, doi: 10.1016/j.actaastro.2019.12.003.